Environmental Studies Faculty Publications   Harry Reid Center for Environmental Studies

11-1998

High-resolution electron time-of-flight apparatus for the soft-x-ray region

Oliver Hemmers
University of Nevada, Las Vegas, Oliver.Hemmers@unlv.edu

S. B. Whitfield
University of Wisconsin - Eau Claire

P. Glans
University of Nevada, Las Vegas

H. Wang
University of Nevada, Las Vegas

Dennis W. Lindle
University of Nevada, Las Vegas, lindle@unlv.nevada.edu

Follow this and additional works at: https://digitalscholarship.unlv.edu/hrc_fac_articles

See next page for additional authors

Part of the Atomic, Molecular and Optical Physics Commons, and the Physical Chemistry Commons

Authors

Oliver Hemmers, S. B. Whitfield, P. Glans, H. Wang, Dennis W. Lindle, R. Wehlitz, and I. A. Sellin

High-resolution electron time-of-flight apparatus for the soft x-ray region

O. Hemmers, S. B. Whitfield, P. Glans, H. Wang, D. W. Lindle et al.

Related Articles

Additional information on Rev. Sci. Instrum.
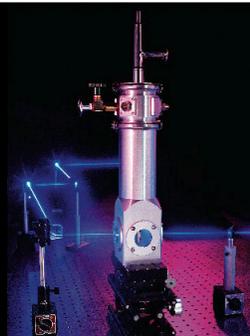
High-resolution electron time-of-flight apparatus for the soft x-ray region

O. Hemmers,[a] S. B. Whitfield,[b] P. Glans,[c] H. Wang, and D. W. Lindle
Department of Chemistry, University of Nevada, Las Vegas, Nevada 89154-4003

R. Wehlitz[d] and I. A. Sellin
Department of Physics, University of Tennessee, Knoxville, Tennessee 37996-1200

A gas-phase time-of-flight (TOF) apparatus, capable of supporting as many as six electron-TOF analyzers viewing the same interaction region, has been developed to measure energy- and angle-resolved electrons with kinetic energies up to 5 keV. Each analyzer includes a newly designed lens system that can retard electrons to about 2% of their initial kinetic energy without significant loss of transmission; the analyzers can thus achieve a resolving power ($E/\Delta E$) greater than 10^4 over a wide kinetic-energy range. Such high resolving power is comparable to the photon energy resolution of state-of-the-art synchrotron–radiation beamlines in the soft x-ray range, opening the TOF technique to numerous high-resolution applications. In addition, the angular placement of the analyzers, by design, permits detailed studies of nondipolar angular distribution effects in gas-phase photoemission. © *1998 American Institute of Physics.* [S0034-6748(98)03611-9]

I. INTRODUCTION

The pulsed nature of synchrotron radiation (SR) emitted from electron or positron storage rings provided the basis for the development, about 25 years ago, of electron-time-of-flight (TOF) spectroscopy as an efficient, but relatively low resolution alternative to electrostatic or magnetostatic analysis. In the TOF technique, kinetic energies are determined by measuring flight times, typically up to several hundred nanoseconds, of electrons traveling a fixed distance between an interaction region and a detector. The method inherently relies on a coincidence between a timing pulse and an electron signal; background noise is suppressed and evenly distributed over the entire time spectrum, greatly simplifying data analysis. Another advantage of the TOF technique is that an entire electron spectrum can be collected simultaneously. In comparison, electrostatic analyzers, even with modern multichannel detection, collect only a portion of an electron spectrum at one time, which in some circumstances renders them susceptible to fluctuations in beam intensity and, in the gas phase, sample pressure. Simultaneous collection of an entire spectrum obviates these fluctuation effects and can increase the measurement efficiency of the electron-TOF method by a significant factor (up to 10^3 in the best of cases) relative to electrostatic analysis.

Early electron-TOF spectrometers were used for photoemission experiments on solid samples where a lower absolute energy resolution could be tolerated. This was often the case in low-energy electron spectroscopy where straightforward retarding-field analysis was sufficient.[1] Since the development of the first electron-TOF spectrometer for gas-phase studies about 20 years ago,[2] improvements have been made in detectors and timing electronics. But more important have been improvements in SR sources, where second- and now third-generation facilities provide significantly shorter light pulses and higher brightness, both factors that can contribute directly to an increase in electron-TOF energy resolution. However, to achieve higher kinetic-energy resolution, and to extend the applicable range of electron-TOF spectroscopy beyond a few hundred electron volts, improvements also are needed in the retarding-lens systems traditionally used in electron-TOF analyzers. Furthermore, brighter, and thus smaller, x-ray beams require more accurate alignment, especially in a rotatable apparatus. This article describes the enhanced resolution and performance of a new electron-TOF system capable of efficient retardation of high-kinetic-energy electrons and easy *in situ* analyzer alignment.

To maintain the relative simplicity of the TOF technique with electron flight times of several hundred nanoseconds, it is necessary to have a sufficient gap between SR light pulses. For example, the third-generation Advanced Light Source (ALS) at the Lawrence Berkeley National Laboratory provides both quasi-continuous and pulsed operation. The ALS is designed to operate with electrons at energies of 1.0–1.9 GeV. Its maximum current is about 400 mA in multibunch mode, in which 287 electron bunches circulate in the storage ring, with a uniform bunch spacing of 2 ns except for one larger gap. In contrast, two-bunch mode at the ALS provides a gap of 328 ns between x-ray pulses; electrons with kinetic energies 5 eV or higher can transit our TOF analyzers within this time window. In two-bunch mode, the maximum current is about 50 mA. The reduction in current relative to multibunch operation is compensated by the enhanced measurement efficiency of the TOF method.

[a] Electronic mail: HEMMERS@NEVADA.EDU
[b] Present address: Department of Physics & Astronomy, University of Wisconsin-Eau Claire, Eau Claire, WI 54702-4004.
[c] Present address: Atomic Physics, Physics Department, Stockholm University, Frescativ. 24, S-10405 Stockholm, Sweden.
[d] Present address: Photon Factory, KEK, High Energy Accelerator Research Organization, 1-1 Oho, Tsukuba, Ibaraki, 305, Japan.
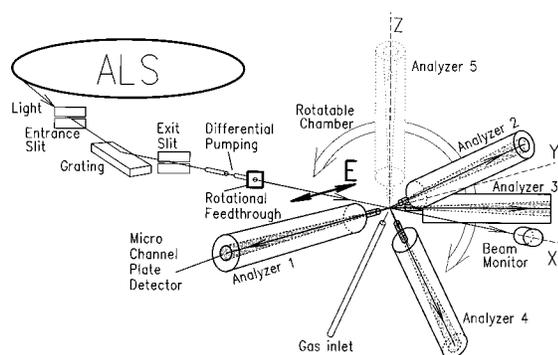
3809

FIG. 1. Experimental schematic of the electron time-of-flight system. Light from the ALS storage ring passes through beamline optics into a differential-pumping section. The chamber and analyzers can rotate around the photon beam for more accurate electron angular-distribution measurements.

II. APPARATUS

Early designs for electron-TOF systems were developed by Bachrach *et al.*[1] for surface-science applications and by White *et al.*[2] for gas-phase samples. The gas-phase design was later improved by Becker *et al.*[3,4] The electron-TOF system described here is a new apparatus that presently has four operational analyzers placed at electron ejection angles shown in Fig. 1. A fifth analyzer is near completion. A novel feature of this apparatus is that analyzers (2) and (3) are positioned 54.7° out of the plane perpendicular to the x-ray beam (the *y*-*z* plane) in order to study nondipolar angular-distribution effects in detail. Analyzers (1) and (4), in the *y*-*z* (or dipole) plane, are used to measure dipolar angular distributions and cross-section ratios. The analyzers are of a new design that includes cylindrical focusing to preserve accurate timing resolution while dramatically improving collection efficiency for highly retarded electrons. To maintain ultimate timing resolution for these new-generation analyzers, significant care was taken in the design of the microchannel-plate detectors and impedance-matched conical anodes. Likewise,

the best commercially available electronic modules were obtained to allow fast simultaneous operation with up to six analyzers. As a result, this new system provides timing and data-collection capabilities that meet or exceed those of other electron-TOF systems in use with SR.

A schematic of the experimental setup is shown in Fig. 1. Light from the storage ring first passes through a soft x-ray beamline for energy selection and focusing. The TOF apparatus was originally designed for ALS bending-magnet beamline 9.3.1 with a photon-energy range of 2–6 keV.[5–7] Before beamline 9.3.1 was completed, the apparatus was tested at bending-magnet beamline 6.3.2[8] and has been used during every ALS two-bunch run since at undulator beamline 8.0.1,[9,10] both of which operate in the 100–1200 eV range. Part of the apparatus is a differential-pumping section adapting the beamline pressure of less than 10^{-6} Pa to the chamber pressure during data collection of 4×10^{-3} Pa.

The vacuum chamber supporting the analyzers can be rotated about the x-ray beam (*x* axis) by ±90°, permitting collection of spectra at many different angles and thereby improving the precision and accuracy of angular-distribution measurements. An in-line rotational feedthrough decouples the chamber rotation from the differential-pumping section while the apparatus is under vacuum. Two gravitational sensors with an operating range of ±45.0° each determine the chamber rotation angle. The exact angular positions of the analyzers can then be calculated for input into the data-analysis procedure. The chamber is aligned with the x-ray beam along its rotational axis in order to avoid movement of the analyzers relative to the interaction region while rotating.

A needle (30 mm long, 50 μm inner diameter, positioned less than 1 mm from the photon beam) directs an effusive jet of sample gas perpendicular to the x-ray beam. The interaction region viewed by the TOF analyzers runs about 3 mm along the x-ray beam and is defined by the beam size in the other dimensions. The gas-inlet assembly, including the needle, is mounted on a three-axis manipulator, and
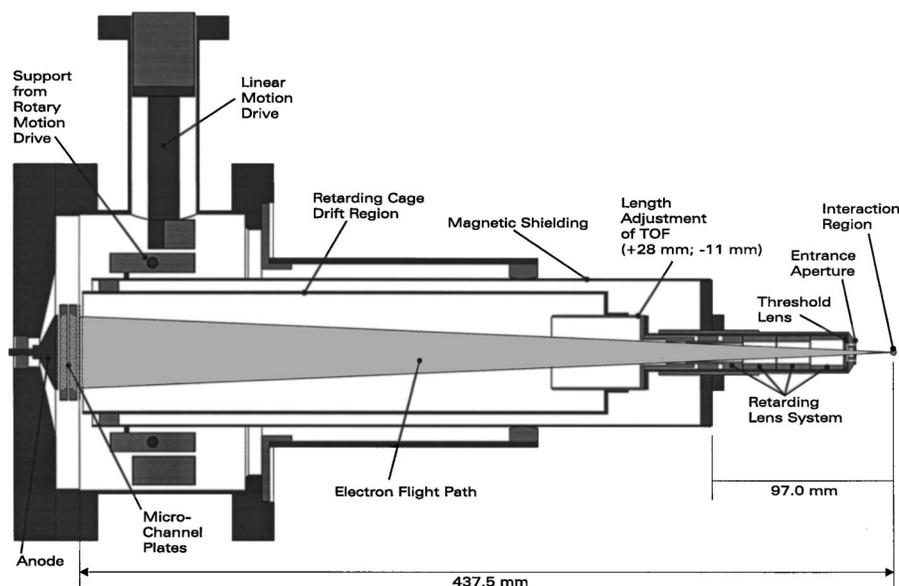

FIG. 2. Cross section of an electron time-of-flight analyzer.

the optimum position of the needle is determined by counting rates in the analyzers. Sample gas enters the gas-inlet assembly through a manual leak valve. A 1000 ℓ/s turbomolecular pump maintains the background pressure, with no sample gas flowing, of less than 10^{-5} Pa. Sample-gas bottles are connected to the leak valve through regulators and other valves providing a backing pressure below an atmosphere to prevent accidental overpressuring. A simple interlock system triggered by set points on the chamber's ion-gauge controller automatically closes valves between the chamber and the differential-pumping section, between the 1000 ℓ/s turbo pump and the roughing pump, and between the chamber and the gas-inlet manifold. High voltages on the microchannel-plate (MCP) detectors also are switched off when the chamber pressure exceeds the set points.

Approximate enhancement of gas pressure in the interaction region relative to the average chamber pressure, due to the use of the needle, has been measured by keeping the pressure at the chamber ion gauge constant while moving the needle about 50 mm away from the photon beam. The count rate typically drops by a factor of 10, suggesting a gas pressure of 4×10^{-2} Pa in the interaction region, which corresponds to a particle density of 10^{10} mm^{-3}.

III. TOF ANALYZERS

Figure 2 shows a cross section of the electron-TOF analyzers. The only vacuum connection between the MCPs inside an analyzer and the main chamber is the 2 mm diam aperture through which electrons enter the analyzer. All analyzers are differentially pumped by a 50 or 80 ℓ/s turbo pump to avoid pressure buildup near the MCPs. Forelines for the turbo pumps are connected to the main vacuum chamber, providing a backing pressure better than what could be obtained with a roughing pump. Efficient differential pumping of the analyzers is important because the recommended operating pressure for MCPs is 10^{-4} Pa, significantly less than the chamber pressure during data collection. Decreasing the MCP operating pressure decreases ion feedback, thereby decreasing background noise.

A straight electron flight path provides fundamental simplicity to the TOF technique, especially in analyzer design. The cylindrically symmetrical analyzers view the same interaction region with the 2 mm entrance apertures at a distance of about 20 mm. The apertures and needle are electrically grounded to maintain a field-free interaction region, an essential attribute for electron angular-distribution measurements. To optimize alignment to a common interaction region, the entrance aperture of each analyzer can be moved *in situ* ±3 mm along two axes perpendicular to the electron flight path, and the length of each analyzer can be adjusted *ex situ* +28 mm/−11 mm from its nominal length.

A total flight path of 437.5 mm and minimum active areas on the MCPs of 41.9 mm diameter yields an angular acceptance of ±2.7°. This corresponds to a solid angle of $2\pi[1-\cos(2.7°)]=7.0\times10^{-3}$ sr, or 1/1800 of the total 4π solid angle. A larger solid angle would increase signal but degrade the angular resolution, as well as energy resolution due to the variation in electron flight length. The actual de-
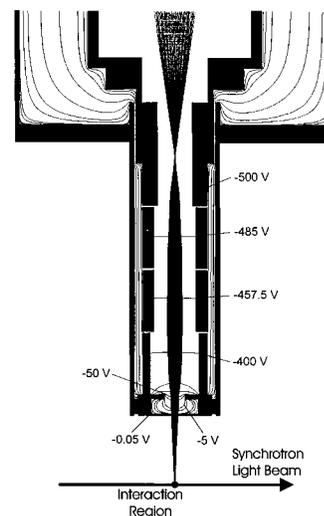

FIG. 3. Cross section of the electron lens system right behind the entrance aperture of the analyzer. The trajectories of electrons with an initial kinetic energy of 505 eV passing through the retarding-lens system were calculated using SIMION software. An applied voltage of −500 V slows the electrons down to a final kinetic energy of 5 eV or about 1% of their initial kinetic energy.

sign is a compromise between expected count rates and energy resolution. Typical flight times can be calculated using $t(\text{ns})=738/\sqrt{E(\text{eV})}$, which yields 738 and 73.8 ns for 1 and 100 eV electrons, respectively. With the time window of 328 ns between pulses in ALS two-bunch mode, a minimum kinetic energy of 5 eV is required for electrons to arrive at the detector before the next x-ray pulse reaches the interaction region. Electrons slower than 5 eV overlap with fast electrons created by the following bunch and complicate the spectra. If desired, the lens system can accelerate electrons to avoid these overlaps.

Figure 3 shows the front end of an analyzer, its lens system, and electron trajectories determined by ray tracing using SIMION software. In this simulation, the electrons begin in the interaction region with a kinetic energy of 505 eV, pass through the entrance aperture, then about 4.0 mm further pass through a second aperture with a diameter of 4.0
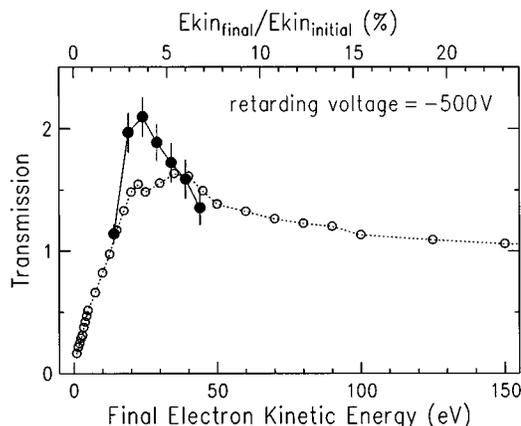

FIG. 4. Simulated (using SIMION-open circles) and measured (filled circles) analyzer transmissions depending on the final electron kinetic energy with an applied retarding voltage of −500 V. The transmission is defined as unity when no voltages are applied, and the electrons fly straight from the interaction region to the detector.
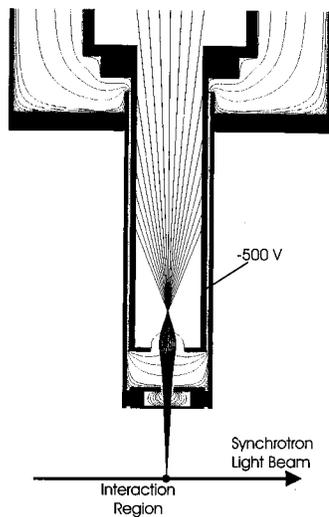
FIG. 5. Previous analyzer design without retarding lens. As in Fig. 3, the initial electron kinetic energy is 505 eV, and the retarding voltage is −500 V. The electrons enter the retarding cage through a large aperture that defocuses the electrons causing a significant loss in transmission.

FIG. 6. Schematic of the data-aquisition electronics. The components AMP to MCA are needed for each analyzer.

mm. The second aperture is usually at ground potential but can be biased with a negative 1–2 V to repel thermal electrons created in experiments with metal–vapor targets. Directly behind the second aperture is the first retardation element of the lens system at a potential of 80% (400 V) of the total retardation voltage of 500 V. The next three elements have 91.5%, 97%, and 100% of the total voltage, respectively. The voltages are applied using a resistor cascade with the following approximate values: 15, 2.2, 1.0, and 0.56 MΩ, totaling 18.76 MΩ. After passing through the lens system, the electrons enter a field-free drift tube with a final kinetic energy of 5 eV. The drift tube extends to the MCP mounting. A coaxial magnetic-shield cylinder made of a Co–Netic AA alloy with a wall thickness of 0.76 mm surrounds the drift tube and reduces the magnetic field inside by a factor of up to 100, typically to about 4 mG. The shielding effect is less near the tube ends.

Trajectories in Fig. 3 exhibit a strong divergence from the analyzer axis, and just 25% of all electrons that pass through the entrance aperture reach the MCPs. The nominal angular acceptance of ±2.7°, valid for electrons retarded to 20% or more of their initial kinetic energy, is reduced to ±0.7° when the retarding voltage slows the electrons down to just 1% of their original kinetic energy. Figure 4 shows the kinetic-energy dependence of the transmission function for 500 V retarding and initial kinetic energies between 500 and 650 eV. The solid circles with error bars in Fig. 4 are from measurements, whereas the open circles connected by a dotted line are from simulations using SIMION, which agree rather well with our measurements. The transmission function, by definition, is unity when no fields are applied and all electrons follow a geometric path into and through the analyzer to the MCPs. Within certain limits, this function scales with energy, e.g., it shows the same behavior for 100 V retarding and electron energies of 100–130 eV. At highly retarded kinetic energies, around 4% of the initial kinetic energy, a pronounced increase in the transmission function
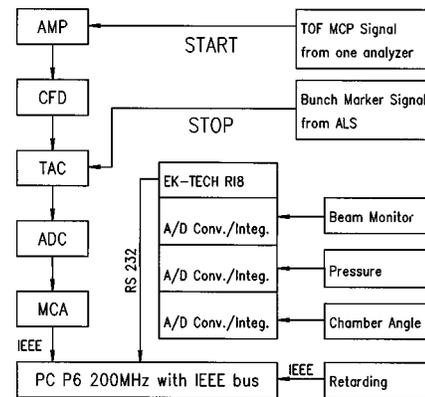
appears. Here, the lens system is focusing electrons that enter the analyzer off axis, effectively increasing the solid angle of acceptance. The steeper increase of the measured points might be due to a distance smaller than the nominal 20 mm between the interaction region and the entrance aperture, thus increasing the acceptance angle for slow electrons more than for fast electrons.

The lowest final kinetic energy measured in Fig. 4 with a transmission greater than one is 14 eV, or 2.7% of the initial kinetic energy. In previous designs,[3,4] the transmission function dropped below one at about 13% of the initial kinetic energy. Figure 5 shows a simulation of a previous design, with no lens system, under the same conditions as in Fig. 3. It is obvious from Fig. 5 that the trajectory density along the analyzer axis is much smaller than in Fig. 3, explaining the reduced transmission. Improved performance due to the new lens system is directly related to an increase in achievable energy resolution (see below). At the lowest kinetic energies, the apparatus is limited by magnetic fields in the inner chamber and the interaction region. Openings in the chamber's magnetic shielding for analyzers and other necessary equipment are responsible for a relatively high residual magnetic field of about 100 mG. Therefore, it is presently difficult to detect electrons with final kinetic energies below 5 eV after retardation. The use of Helmholtz coils to compensate the earth's magnetic field is being considered to alleviate this problem.

IV. DETECTOR

Electrons are detected by two MCPs (Galileo Model No. 1390-4000, 50.0 mm diameter, minimum active diameter of 41.9 mm, outside contact rim, 8° bias angle, 10 μm channel diameter, 12 μm pore distance center to center, 0.46 mm thick) in a Chevron arrangement. The upper limit of MCP detection efficiency for slow electrons ($<$50 eV) is based on the area ratio of all pores to the total active area and is 57% for the above-mentioned MCPs. A honeycomb-etched grid with a transmission of 92% in front of the first MCP accelerates all incoming electrons by 500 V to increase detection efficiency of slow electrons; in this way, efficiency can reach 85% because electrons striking the interstitial material can

produce secondary electrons which can excite neighboring channels. General information about MCPs and MCP-based detectors can be found elsewhere.[11]

An early design of the MCP mounting employed a resistor–divider chain with a total resistance of 66.7 MΩ, but due to uncertainties in MCP resistances, which range between 50 and 100 MΩ, it was necessary to apply voltages up to 4000 V to reach MCP operating voltages of 9000–1000 V. The present design employs a resistor–divider chain with a total resistance of 10 MΩ and an operating voltage of not more than 3000 V. Voltage is applied to each MCP through a stainless-steel ring on one side and a brass contact ring with contact fingers on the other side. The bent fingers apply a small force to the MCP to improve electrical contact. Kapton insulator rings (0.125 mm thick) are placed between the contact rings. A voltage of 200 V is applied between the MCPs, which are separated by 0.6 mm. After a total amplification of about 10^7, emerging electrons are accelerated onto a conical anode by 300 V. The 50 Ω impedance-matched anode is held at a potential of 3000 V, and decoupling capacitors of 470 or 1000 pF are used to generate 10–100 mV pulses with a full width at half maximum (FWHM) of 1–2 ns. The dark-count rate of the detector is typically $20–50 \text{ s}^{-1}$, depending on MCP voltage, gas pressure, and retarding voltages, and is distributed randomly over 4096 channels in the spectrum.

Figure 6 shows a schematic of the electronics for processing MCP pulses from one TOF analyzer. Mounted on the analyzer is a surge protector (e.g., Phillips Scientific Model No. 450) to protect the wideband fast-pulse preamplifier (Phillips Scientific Model No. 6954). The preamplifier (AMP) has a bandwidth of up to 1.8 GHz and a voltage gain of 50. A 200 MHz quad constant-fraction discriminator (CFD) with a modified internal delay for fast MCP pulses (Tennelec/Oxford Model TC 454) generates precision timing signals from the fast negative output signals of the AMP and supports four channels. We also have used the EG&G Ortec 1 GHz amplifier and timing discriminator model No. 9327, which combines the AMP and CFD into one unit.

The CFD output signal is the start signal for a Tennelec 200 MHz time-to-amplitude converter/biased amplifier (TAC/biased amp, model TC864). The TAC provides a 0–10 V full-scale output signal proportional to the time difference between ''Start'' and ''Stop''. The time window is optimized for the ALS bunch spacing of 328 ns. The ''Stop'' signal is provided by the ALS as a negative NIM pulse (−0.8 V) every 656 ns. The bunch-marker signal jitters and is at the moment our main limitation for timing resolution. Furthermore, the fact that the bunch marker has a period twice that of the x-ray pulses creates two spectra shifted by 328 ns, limiting the total channels in a spectrum to 4096 instead of a possible 8192. The TAC analog–output voltage is converted into a channel number with a fast, 800 ns, fixed-dead-time, analog-to-digital converter (ADC), model 8715 from Canberra. This ADC has a maximum channel resolution of 8192 and is operated in the pulse-height-analysis and anticoincidence modes. The digital ADC output signal feeds into a multichannel analyzer (MCA) from Tennelec/Oxford (model PCA-Multiport-E), which supports up to 16 384
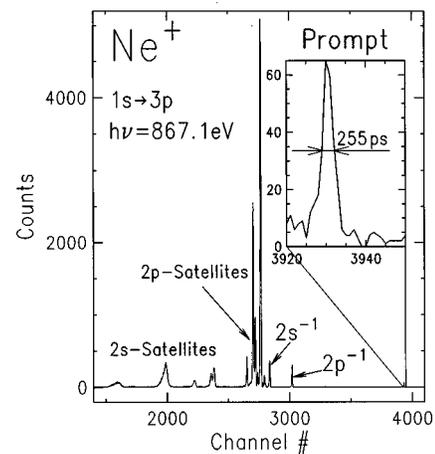

FIG. 7. Electron time-of-flight spectrum taken on the Ne $1s \rightarrow 3p$ resonance at 867.1 eV. The FWHM of the ''prompt'' (260 ps) determines the total timing resolution of the analyzer and electronics.

channels from an external ADC and can store up to 16 777 215 counts per channel. Figure 6 shows just one AMP-to-MCA set of electronics; each analyzer needs its own set. All the MCAs are read through an IEEE-488 interface by an IBM-compatible computer-interface board (AT-GPIB/TNT, Plug and Play) from National Instruments inside a Pentium-based PC Data-acquisition software is written using the LABVIEW programming language from National Instruments.

Analog signals from the beam monitor, the chamber pressure, and the gravitational sensors are converted to digital signals and integrated, where applicable, with a remote interface (RI8) from EKTECH. A serial connection (RS 232) links the RI8 to the data-acquisition computer to monitor and store these values. The retarding/accelerating voltages of up to ±1000 V are applied with a Keithley Electrometer (Model 6517A) controlled remotely through an IEEE connection from the computer. Additionally, it is used to measure current from the beam monitor.

V. PERFORMANCE

Kinetic-energy resolution, $\Delta E/E$, in an electron-TOF spectrum is given by

$$\frac{\Delta E}{E} = \sqrt{\left(\frac{2\Delta t}{t}\right)^2 + \left(\frac{2\Delta l}{l}\right)^2 + \left(\frac{\Delta \lambda}{\lambda}\right)^2} \qquad (1)$$

and depends on the uncertainties in the wavelength ($\Delta\lambda/\lambda$), the flight time ($\Delta t/t$), and the electron flight-path length ($\Delta l/l$). The latter is determined by the size of the interaction region, typically 100–1000 μm, the analyzer acceptance angle, and the variation in length of all possible flight paths. Due to the small acceptance angle, the length of the flight path only varies between 437.5 and 438.0 mm. This variation limits the overall analyzer resolution, $\Delta E/E$, to 0.2% or more even for a point-size interaction region. The actual size of the interaction region, which depends on the focusing of the x-ray beam, is about 1.0 mm wide and 1.0 mm high at BL 8.0.1. Beamline optics provide a better focus (100 μm diameter) at a point 1.5 m upstream, a spot unavailable to our
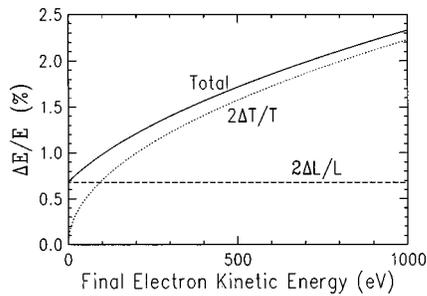
FIG. 8. Total analyzer resolution [neglecting $\Delta\lambda/\lambda$ in Eq. (1)] depending on the final electron kinetic energy. The individual components for time, with $\Delta t = 255$ ps, (dotted line) and flight path, with $\Delta l = 1.5$ mm, (dashed line) are shown.

apparatus because it is within another experimental setup. Therefore, the present limit for total analyzer resolution at BL 8.0.1 is 0.7% of the final kinetic energy.

Timing uncertainties are due to contributions from the duration of the synchrotron light pulse (49 ps FWHM at 1 mA bunch current and 82 ps FWHM at 20 mA for ALS two-bunch mode at a ring energy of 1.9 GeV), the detector ($<$60 ps), electronics ($<$130 ps), and the stop signal provided by the ALS (100–300 ps, depending on the beamline, cable delays, and signal splitters). The ALS staff is working on improving the stop signal to about 50 ps and on providing an electronic delay. Either a very fast photoline or the ''prompt'' signal resulting from Rayleigh scattering can be used to measure timing resolution directly. Using the prompt has the advantage that the size of the interaction region can be neglected because light travels through it in 3 ps. (A fast photoline such as He $1s$ with a kinetic energy of 700 eV gains an additional 60 ps FWHM because of the size of the interaction region.) Both an ion-TOF spectrometer[7] and the electron-TOF spectrometer described here, using the same electronics, have indicated a timing-resolution limit of about 200 ps. This limit is presently hard to reach at beamline 8.0.1 due to jitter in the stop signal. More typical values range between 250 and 350 ps.
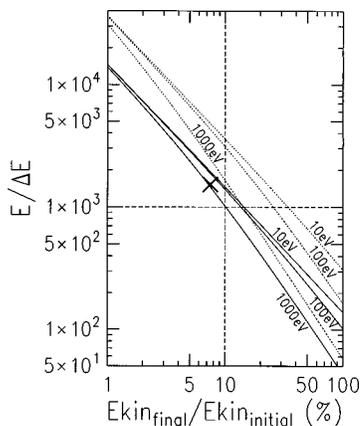

FIG. 9. Total analyzer resolving power [neglecting $\Delta\lambda/\lambda$ in Eq. (1)] relative to the ratio between the final electron kinetic energy and the initial kinetic energy for different (10, 100, and 1000 eV) initial kinetic energies (solid lines). The cross marks the analyzer resolving power for the $2p^{-2}(^1D)3p$ photoline shown in Fig. 10. The dotted lines are derived for optimal conditions with $\Delta t = 200$ ps and an interaction region spot size of 100 μm (Δl = 0.6 mm including the flight-path uncertainty of 0.5 mm).
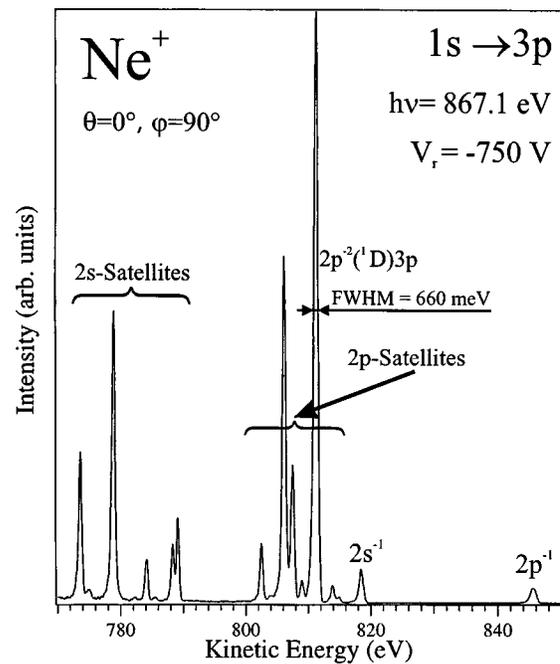

FIG. 10. Same spectrum as shown in Fig. 7 after time-to-energy conversion.

Figure 7 shows a neon spectrum taken at the $1s \rightarrow 3p$ resonance (867.1 eV) with flight time on the x axis and total counts on the y axis. The spectrum was collected for 200 s with a ring current of 20 mA. The entrance and exit slits were set at 50 μm, and the monochromator grating provided a bandpass of 650 meV, corresponding to a photon resolution of 1350. The analyzer was positioned parallel to the plane of the storage ring ($\theta = 0°$) and perpendicular to the photon beam ($\phi = 90°$). A retarding voltage of -750 V was applied to reduce the initial electron kinetic energies by 89%–97%. The fastest signal, at channel number 3930, is the prompt, which indicates a timing resolution of 255 ps.

It is important to note that $\Delta l/l$ and Δt are constant, however $\Delta t/t$ varies with kinetic energy as shown in Fig. 8. For kinetic energies less than 100 eV, $\Delta l/l$, with $\Delta l = 1.5$ mm, limits the analyzer resolution more than $\Delta t/t$ with $\Delta t = 255$ ps. At 100 eV, the total analyzer resolution is 1% of the final kinetic energy, mainly due to Δl. For faster electrons, $\Delta t/t$ increases, and for a kinetic energy of 700 eV the analyzer resolution reaches 2% (14 eV). These numbers make it clear how important a well-designed retarding system is for improving analyzer resolution and overall resolving power.

Overall analyzer resolution also is dependent on initial electron kinetic energies, as shown in Fig. 9. The three solid lines for 10, 100, and 1000 eV illustrate analyzer resolving powers for retardations down to 1% of the initial kinetic energies, e.g., retarding a 1000 eV electron to 10 eV final kinetic energy. Retardation of 90% is necessary to achieve an analyzer resolving power ($E/\Delta E$) of at least 1000, and, as seen in Fig. 4, a retardation of 98% is possible without significant loss in transmission. As mentioned above, BL 8.0.1 is able to provide a spot size of 100 μm$\times$100 μm and a timing resolution of 200 ps will be possible when the ALS provides a better quality stop signal. With these improve-

ments, the analyzer resolution and resolving power will improve significantly (dotted lines in Fig. 9); total resolving powers of 10 000 will be feasible. The cross in Fig. 9 marks the analyzer resolving power for the $2p^{-2}(^1D)3p$ line shown in Fig. 10 that was retarded to 7.5% of its initial energy. Figure 10 shows the same spectrum as in Fig. 7, but with the time axis converted to a kinetic-energy axis. Photoelectrons of the $2p^{-2}(^1D)3p$ line with an initial kinetic energy of 811 eV have been retarded by 750 V to a final kinetic energy of 61 eV. The resonant photoline $2p^{-2}(^1D)3p$ has a FWHM of 660 meV. With a fine-structure splitting of 60 meV and a lifetime width of the Ne $1s$ hole state of Γ_{1s} = 220 meV,[12] an analyzer resolution of 550 meV is deduced. This corresponds to a total analyzer resolution of 0.9%, or a resolving power of over 1500.

VI. DATA ANALYSIS

The present system was built to measure angular distributions of photo- and Auger electrons. In general, no absolute measurements are performed using the TOF technique. To calibrate measurements of unknown angular distributions, gases with well-characterized photo- and Auger lines are measured under the same, or as similar as possible, conditions to determine transmission functions and relative analyzer efficiencies. Therefore, sizes and shapes of the interaction region or fluctuations in the target–gas pressure and beam intensity that would affect absolute measurements are accounted for with relative measurements.

Electron angular-distribution measurements strongly depend on the degree of linear polarization, i.e., the first Stokes parameter and the tilt of the polarization vector with respect to the plane of the storage ring. These two parameters are determined by measuring the intensity ratio of the Ne $2s$ and $2p$ valence lines at about 20 different angles perpendicular to the photon beam (to eliminate the influence of first-order nondipole effects). The Ne $2s\beta$ parameter has a value of two and is sufficient to fit a curve through the measured ratios to determine the polarization parameters as well as the Ne $2p\beta$ parameter and the Ne $2s$ and $2p$ cross-section ratio. The polarization parameters are slightly photon-energy dependent and have to be determined for the region of interest. However, the degree of linear polarization at BL 8.0.1 is always higher than 99% and the tilt is usually not more than 1°.

A more complex part of the data analysis is time-to-energy conversion of the spectra (see Figs. 7 and 10). Time spectra are not linear in energy and thus simple Gaussian line shapes are asymmetric, especially at low kinetic energies. When it is necessary to fit several peaks to a group of lines, it is important to make the spectrum linear in energy without affecting peak areas. The relationship between the flight time t and the kinetic energy E_{kin} of an electron under field-free conditions is given by

$$E_{kin} = \frac{1}{2} m v^2 = \frac{ml^2}{2} \times \frac{1}{t^2}, \tag{2}$$

with m being the electron mass and l being the distance from the interaction region to the detector. Most spectra are measured with a retarding voltage, and Eq. (2) cannot be applied
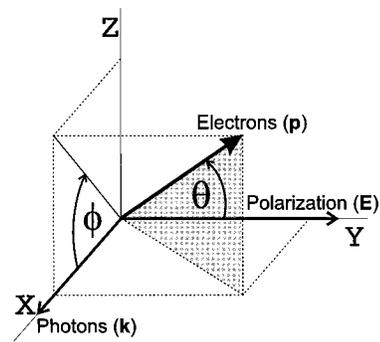

FIG. 11. Geometry applicable to photoelectron angular-distribution measurements using polarized light. Θ is the polar angle between the photon polarization vector E and the momentum vector p of the photoelectrons. ϕ is the azimuthal angle defined by the photon propagation vector k and the projection of p into the x-z plane.

without precise knowledge of all the electrical potentials in the analyzer; analytical use of Eq. (2) is not feasible, and an empirical method must be used in which a kinetic energy is assigned to every channel in the spectrum. Using the energy calibration of the x-ray monochromator, channel positions of photolines are measured at different photon energies to get a data set of about 20–40 points. By energy conservation, differences between photon energies and binding energies are the final electron kinetic energies and can be assigned to appropriate channels. Connection between a channel in the time spectrum (ch) and flight time (t) is accomplished using channel position of the prompt: $t \propto (\text{prompt-ch})$. Equation (2) can be rewritten as

$$E_{kin}(\text{ch}) \propto \frac{1}{(\text{prompt} - \text{ch})^2}. \tag{3}$$

The next step is to linearize this data set by plotting the square root of $1/(\text{prompt-ch})^2$ with respect to the kinetic energy (E_{kin}) and fitting a straight line through the points. If the prompt peak is not visible in the spectrum, it is possible to determine its position by trying different channel numbers where the prompt is expected. Because there is just one straight line possible through the measured data set, the prompt position can be determined to better than 0.1 channel. The linear-fit function is then transformed back, assigning every channel an energy value. All time spectra taken with the same retarding voltages can now be converted into energy spectra. The following normalization is used to correct peak areas during this conversion because point density in energy spectra increases with decreasing kinetic energies:

$$I = \frac{c(\text{ch}) - b}{E(\text{ch}+1) - E(\text{ch})}. \tag{4}$$

In Eq. (4), I is the intensity in the energy spectrum at kinetic energy $E(\text{ch})$, b is the background count rate in the time spectrum, and $c(\text{ch})$ is the count rate in channel ch of the time spectrum. Changes in widths and heights are obvious when comparing the slowest lines in Fig. 7 with the same lines energy converted in Fig. 10.

Time-to-energy conversion gets more complicated for energies below 5 eV because the electrons are strongly in-

fluenced by magnetic fields, and the kinetic-energy axis cannot be determined accurately with a linear fit. It is necessary to use a polynomial fit function and to smoothly add it to the linear fit to obtain a complete and accurate time-to-energy conversion.

VII. APPLICATIONS

In order to measure photoelectron angular distributions, up to six electron-TOF analyzers can be positioned at several combinations of the angles θ and ϕ (see Fig. 11) in a vacuum chamber which can rotate about the x-ray beam. Four analyzers have been used to date. The differential cross section for photoemission processes within the nonrelativistic dipole approximation is given by[13]

$$\frac{d\sigma}{d\Omega} = \frac{\sigma}{4\pi}\left(1 + \frac{\beta}{2}\left(3\cos^2\theta - 1\right)\right), \tag{5}$$

which describes the angular distribution of photoelectrons ejected from a randomly oriented sample by 100% linearly polarized light. Here, σ is the partial photoionization cross section, and Ω is the solid angle. In the dipole approximation, the parameter β completely describes the angular distribution of photoelectrons. From Eq. (5), it can be shown that photoelectron peak intensities are independent of the β parameter at the so-called magic angle, $\theta_m \approx 54.7°$. The present electron-TOF apparatus was designed to measure higher-order corrections to the dipole approximation, described by the parameters γ and δ, and given by[14]

$$\frac{d\sigma}{d\Omega} = \frac{\sigma}{4\pi}\left(1 + \frac{\beta}{2}\left(3\cos^2\theta - 1\right)\right.$$
$$\left. + (\delta + \gamma\cos^2\theta)\sin\theta\cos\phi\right) \tag{6}$$

for 100% linearly polarized light. Thus, the chamber includes two analyzers (2 and 3) mounted out of the *y-z* plane (Fig. 1), a geometry which permits direct and sensitive measurement of the nondipole angular-distribution parameters (γ and δ) for photoelectrons. Furthermore, the apparatus is designed so that when analyzer (1) is at $\theta=0°$ and $\phi=90°$, analyzer (2) is at $\theta=90°$ and $\phi=35.3°$, analyzer (3) is at $\theta_m=54.7°$ and $\phi=0°$ (*the nondipole magic-angle analyzer*), and analyzer (4) is at $\theta_m=54.7°$ and $\phi=90°$ (*the dipole magic-angle analyzer*). Peak intensities in the dipole magic-angle analyzer, in the *y-z* plane ($\phi=90°$), are independent of the nondipole parameters γ and δ [see Eq. (6)], as well as the dipole parameter β. In contrast, peak intensities in the nondipole magic-angle analyzer are independent of the dipole parameter β, but depend on γ and δ.

Analyzer (2) allows direct determination of δ because at $\theta=90°$ the γ dependence vanishes and the peak intensities just depend on δ and β. With a planned fifth analyzer at $\theta=90°$ and $\phi=90°$, it will be even easier to determine δ by comparison with analyzer (2). Both analyzers will measure the same intensities due to β but different intensities based on δ. The placement of the analyzer ports is excellent for determining all three angular distribution parameters without rotating the chamber. The option of a sixth analyzer posi-

tioned at $\theta=180°$ and $\phi=90°$ would be redundant to the analyzer at $\theta=0°$ and $\phi=90°$ and does not provide more information for angular-distribution measurements. Nevertheless, it will be useful for electron–electron coincidence measurements, as described by Viefhaus *et al.*[15,16]

With this apparatus, angular distributions of valence photoelectrons showing effects due to higher-multipole interactions have been measured for the first time.[17,18] The experiments were performed on Ne 2s and 2p throughout the 250–1200 eV photon-energy range. Furthermore, it was possible to prove the breakdown of the independent-particle approximation throughout the same range.[19] Other measurements include the photon-energy dependence of ionization excitation in helium at medium energies (90–900 eV),[20] where we measured the photoionization-excitation-to-photoionization ratio for He$^+$ nl ($n=2-6$) and determined asymptotic high-energy ratios for He$^+$ nl ($n=2-5$) which agree with theoretical predictions.[21]

Current research projects include nondipole angular-distribution measurements in Xe and small molecules such as N_2. We have observed a strong resonance-like increase in the value of the γ parameter about 60 eV above the N_2 1s ionization threshold, which causes an angular-distribution effect about 20 times more pronounced than predicted by theory for atomic nitrogen. Other projects include electron angular-distribution measurements of the Ar 2s satellite lines as well as the Ne valence lines in the Ne $1s \rightarrow 3p$ resonance region.

In conclusion, we have described the development of significantly improved electron-TOF analyzers for gas-phase samples and the design of an apparatus for angle-resolved-photoemission experiments to study dipole and nondipole angular-distribution effects. The new retarding-lens system increases the resolving power to up to 10 000 for high-kinetic-energy electrons. These improved electron-TOF analyzers are an alternative to electrostatic analyzers while maintaining the advantages of electron-TOF spectroscopy: constant background, large energy window, and independence of varying gas-target pressures and fluctuations in the beam intensity. A high-brilliance light source like the ALS with submillimeter beam sizes, combined with this type of electron-TOF analyzer, provides state-of-the-art instrumentation for high-resolution angle-resolved photoelectron spectroscopy.

[1] R. Z. Bachrach, F. C. Brown, and S. B. M. Hagström, J. Vac. Sci. Technol. **12**, 309 (1975).

[2] M. G. White, R. A. Rosenberg, G. Gabor, E. D. Poliakoff, G. Thornton, S. H. Southworth, and D. A. Shirley, Rev. Sci. Instrum. **50**, 1268 (1979).

[3] U. Becker, D. Szostak, H.-G. Kerkhoff, M. Kupsch, B. Langer, R. Wehlitz, A. Yagishita, and T. Hayaishi, Phys. Rev. A **39**, 3902 (1989).

[4] U. Becker and R. Wehlitz, Phys. Scr. **41**, 127 (1992).

[5] G. Jones, S. Ryce, D. W. Lindle, B. A. Karlin, J. C. Woicik, and R. C. C. Perera, Rev. Sci. Instrum. **66**, 1748 (1995).

[6] R. C. C. Perera, G. Jones, and D. W. Lindle, Rev. Sci. Instrum. **66**, 1745 (1995).

[7] W. Ng, G. Jones, R. C. C. Perera, D. Hansen, J. Daniels, O. Hemmers, P. Glans, S. Whitfield, H. Wang, and D. W. Lindle, Rev. Sci. Instrum. **67**, 1 (1996).

[8] J. H. Underwood, E. M. Gullikson, M. Koipe, P. J. Batson, P. E. Denham, K. D. Franck, R. E. Tackaberry, and W. F. Steele, Rev. Sci. Instrum. **67**, 3372 (1996).

[9] R. C. C. Perera, Nucl. Instrum. Methods Phys. Res. A **319**, 277 (1992).

[10] J. J. Jia, T. A. Callcott, J. Yurkas, A. W. Ellis, F. J. Himpsel, M. G. Samant, J. Stöhr, D. L. Ederer, J. A. Carlisle, E. A. Hudson, L. J. Terminello, D. K. Shuh, and R. C. C. Perera, Rev. Sci. Instrum. **66**, 1394 (1995).

[11] J. L. Wiza, Nucl. Instrum. Methods **162**, 587 (1979).

[12] L. Avaldi, G. Dawber, R. Camilloni, G. C. King, M. Roper, M. R. F. Siggel, G. Stefani, M. Zitnik, A. Lisini, and P. Decleva, Phys. Rev. A **51**, 5025 (1995).

[13] S. T. Manson and D. Dill, in *Electron Spectroscopy: Theory, Techniques and Applications*, edited by C. R. Brundle and A. D. Baker (Academic, New York, 1978), Vol. 2, p. 157.

[14] J. W. Cooper Phys. Rev. A **47**, 1841 (1993).

[15] J. Viefhaus, L. Avaldi, G. Snell, M. Wiedenhöft, R. Hentges, A. Rüdel, F. Schäfers, D. Menke, U. Heinzmann, A. Engelns, J. Berakdar, H. Klar, and U. Becker, Phys. Rev. Lett. **77**, 3975 (1996).

[16] J. Viefhaus, G. Snell, R. Hentges, M. Wiedenhöft, F. Heiser, O. Geßner, and U. Becker, Phys. Rev. Lett. **80**, 1618 (1998).

[17] O. Hemmers, G. Fisher, P. Glans, D. L. Hansen, H. Wang, S. B. Whitfield, R. Wehlitz, J. C. Levin, I. A. Sellin, R. C. C. Perera, E. W. B. Dias, H. S. Chakraborty, P. C. Deshmukh, S. T. Manson, and D. W. Lindle, J. Phys. B **30**, L727 (1997).

[18] D. W. Lindle, O. Hemmers, P. Glans, D. L. Hansen, H. Wang, S. B. Whitfield, R. Wehlitz, J. C. Levin, I. A. Sellin, and R. C. C. Perera, Indian J. Phys., B **71B**, 325 (1997).

[19] E. W. B. Dias, H. S. Chakraborty, P. C. Deshmukh, S. T. Manson, O. Hemmers, P. Glans, D. L. Hansen, H. Wang, S. B. Whitfield, R. Wehlitz, J. C. Levin, I. A. Sellin, R. C. C. Perera, and D. W. Lindle, Phys. Rev. Lett. **78**, 4553 (1997).

[20] R. Wehlitz, I. A. Sellin, O. Hemmers, S. B. Whitfield, P. Glans, H. Wang, D. W. Lindle, B. Langer, N. Berrah, J. Viefhaus, and U. Becker, J. Phys. B **30**, L51 (1997).

[21] J.-Z. Tang and J. Burgdörfer, J. Phys. B **30**, L523 (1997).